

REPORT

SUPERCONDUCTIVITY

Spatial control of heavy-fermion superconductivity in CeIrIn₅

Maja D. Bachmann^{1,2*}, G. M. Ferguson^{3*}, Florian Theuss³, Tobias Meng⁴, Carsten Putzke^{1,5}, Toni Helm¹, K. R. Shirer¹, You-Sheng Li^{1,2}, K. A. Modic¹, Michael Nicklas¹, Markus König¹, D. Low³, Sayak Ghosh³, Andrew P. Mackenzie^{1,2}, Frank Arnold¹, Elena Hassinger^{1,6}, Ross D. McDonald⁷, Laurel E. Winter⁷, Eric D. Bauer⁷, Filip Ronning⁷, B. J. Ramshaw³, Katja C. Nowack^{3,8††}, Philip J. W. Moll^{1,5††}

Although crystals of strongly correlated metals exhibit a diverse set of electronic ground states, few approaches exist for spatially modulating their properties. In this study, we demonstrate disorder-free control, on the micrometer scale, over the superconducting state in samples of the heavy-fermion superconductor CeIrIn₅. We pattern crystals by focused ion beam milling to tailor the boundary conditions for the elastic deformation upon thermal contraction during cooling. The resulting nonuniform strain fields induce complex patterns of superconductivity, owing to the strong dependence of the transition temperature on the strength and direction of strain. These results showcase a generic approach to manipulating electronic order on micrometer length scales in strongly correlated matter without compromising the cleanliness, stoichiometry, or mean free path.

The electronic ground state of heavy fermions sensitively depends on the coupling between a localized state and an itinerant electronic system. As the coupling strength is tuned, metallic, superconducting, or magnetically ordered phases are induced, yielding the rich phase diagrams typical for materials of this class. This tunability could be exploited for device-based applications if the electronic order can be locally controlled within a crystalline sample: Metallic, magnetic, or superconducting regions could be induced within a single crystal by precise spatial control over the tuning parameter. Strain is a particularly powerful way to achieve this goal: It introduces no disorder, and its independent components offer multiple degrees of freedom to couple to electronic order. Most commonly, uniform uniaxial strain (*1*) or biaxial strain (*2*) is applied. In this work, we demonstrate micrometer-scale control over the superconducting order in stoichiometric and ultraclean CeIrIn₅ by inducing a nonuniform

tailored strain field in microstructured single-crystal devices. Our experimental approach exploits strain induced by differential thermal contraction between the sample and the substrate, as well as our submicrometer control over the shape of the sample. The tetragonal

heavy-fermion metal CeIrIn₅ exhibits material parameters that are ideal for establishing spatial control of a correlated state [Sommerfeld coefficient $\gamma \sim 720 \text{ mJ mol}^{-1} \text{ K}^{-2}$ (*3*), effective mass $m^* \sim 30m_e$, where m_e is the mass of an electron (*4*)]. The superconducting transition temperature, T_c , of this material is highly sensitive to strain, owing to the strong dependence of Ce 4f hybridization on the Ce-Ce interatomic distance. Straining the sample along the *a* direction increases the bulk superconducting transition temperature ($T_{c0} = 400 \text{ mK}$) by $56 \text{ mK/kbar} \sim 14\% T_{c0}/\text{kbar}$, whereas compression along the *c* direction decreases it at the rate of $-66 \text{ mK/kbar} \sim -16.5\% T_{c0}/\text{kbar}$ (*5, 6*). Although uniaxial strain strongly alters T_c , the almost equal but opposite effects of *a*- and *c*-direction strain lead to an overall weak change of T_c under hydrostatic pressure ($10 \text{ mK/kbar} \sim 2.5\% T_{c0}/\text{kbar}$) (*7*). For a crystal subjected to a nonuniform strain field, complex patches of superconductivity are expected to appear within the heavy Fermi liquid.

Figure 1 illustrates nonuniform superconductivity for the simple case of a rectangular slab also referred to as a lamella. The lamella ($150 \mu\text{m}$ by $30 \mu\text{m}$ by $2 \mu\text{m}$) was carved from a macroscopic crystal by using focused ion beam (FIB) machining [for fabrication details, see (*8-10*)] and was joined to the sapphire substrate with a thin layer of epoxy (approximately

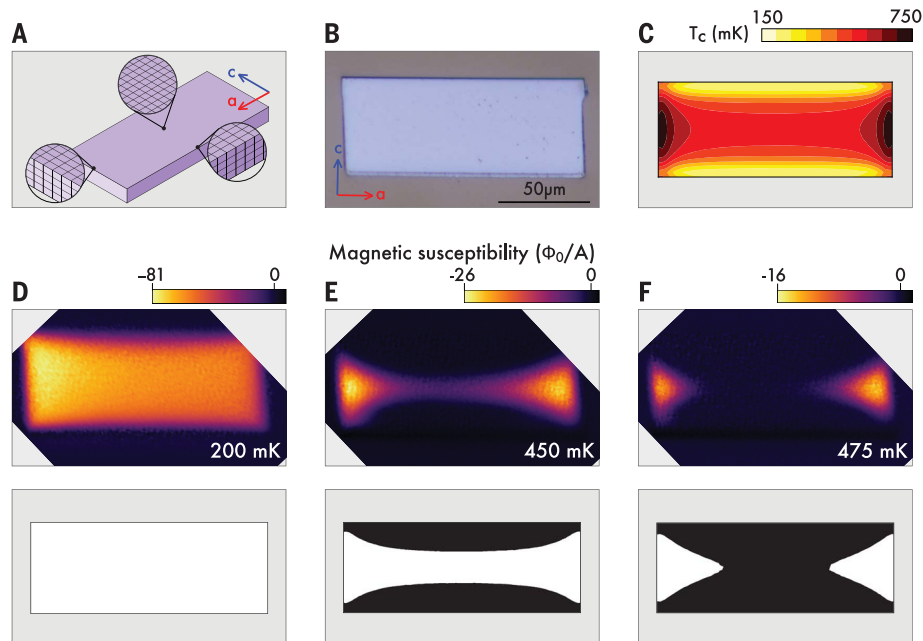


Fig. 1. The superconducting transition in a lamella under biaxial strain. (A) Sketch of the distortion of a thin lamella of CeIrIn₅ coupled to sapphire at low temperatures. (B) Optical image of a 2- μm -thick lamella cut by FIB machining in the (*a*, *c*) plane. (C) Finite element simulation of the T_c map across the sample, arising from the strain profile and strain dependence of T_c (*10*). (D–F) (Top) Local susceptibility images at three representative temperatures. A negative diamagnetic susceptibility indicates superconducting regions of the sample. The susceptibility is measured in units of superconducting magnetic flux quanta (Φ_0) detected in the SQUID per ampere (A) applied to the field coil. (Bottom) Superconducting regions (white) calculated from the strain profile in the device, corresponding to constant temperature contours of the T_c map in (C).

¹Max Planck Institute for Chemical Physics of Solids, D-01187 Dresden, Germany. ²School of Physics and Astronomy, University of St. Andrews, St. Andrews KY16 9SS, UK.

³Laboratory of Atomic and Solid State Physics, Cornell University, Ithaca, NY 14853, USA. ⁴Institute for Theoretical Physics, Technical University Dresden, D-01062 Dresden, Germany. ⁵Institute of Material Science and Engineering, École Polytechnique Fédérale de Lausanne (EPFL), 1015 Lausanne, Switzerland. ⁶Physik-Department, Technische Universität München, Garching, D-85748 Germany. ⁷Los Alamos National Laboratory, Los Alamos, NM 87545, USA. ⁸Kavli Institute at Cornell for Nanoscale Science, Cornell University, Ithaca, NY 14853, USA.

*These authors contributed equally to this work.

†These authors contributed equally to this work.

††Corresponding author. Email: philip.moll@epfl.ch (P.J.W.M.); kcn34@cornell.edu (K.C.N.)

a few hundred nanometers thick). This epoxy is substantially softer than the crystalline substrate and the sample; finite element modeling corroborates the intuitive assumption that the differential thermal contraction transmitted through the epoxy is largely independent of the exact details of the glue layer, such as its thickness or elastic moduli [see (10) for details]. The crystallographic c direction is aligned with the short side of the lamella and the a direction with the long side. The use of sapphire cut along the (0001) surface ensures isotropic thermal contraction of the substrate. Whereas sapphire is known for its low thermal contraction, CeIrIn₅ contracts strongly upon cooling, as is typical of many Ce-based compounds (11). As a result, the sample is under tensile strain at low temperature.

To study the superconducting transition in the lamella, we use scanning superconducting quantum interference device (SQUID) micros-

copy (SSM) to image the diamagnetic response of the sample with micrometer-scale resolution. To detect superconductivity, we apply a local magnetic field by sourcing a current through a $\sim 6\text{-}\mu\text{m}$ field coil integrated on the SQUID chip. The $\sim 1.5\text{-}\mu\text{m}$ SQUID pickup loop detects the local magnetic susceptibility measured in magnetic flux per unit current in the field coil [see (10) for details]. Superconducting regions of the sample exhibit a strong diamagnetic response, which enables us to distinguish them from metallic and insulating regions.

Susceptibility images as a function of temperature (top images in Fig. 1, D to F) reveal that superconductivity first emerges at the short edges while most of the lamella remains metallic. As the temperature is lowered, larger fractions of the lamella become superconducting, thus leading to the growth of triangular superconducting patches protruding into the

lamella, which eventually join in the center (Fig. 1E). At even lower temperatures, the order parameter remains suppressed on the long edge. The observation of superconductivity at the edge of the sample before the interior is unexpected. Usually, for a thin superconducting slab cooled in Earth's magnetic field, the demagnetization factor at the sample edges initially favors the appearance of superconductivity in the center of the sample (12).

Before analyzing the spatial pattern in the images, we estimate whether strain caused by differential thermal contraction combined with the strain sensitivity of T_c in CeIrIn₅ can cause the observed variations in T_c of several hundred millikelvin. When cooled to cryogenic temperatures, CeIrIn₅ and sapphire contract by ~ 0.3 and $\sim 0.08\%$, respectively. Given this mismatch, we expect strain on the order of 0.1% to exist within the CeIrIn₅ crystal at low temperature. Using a typical elastic modulus

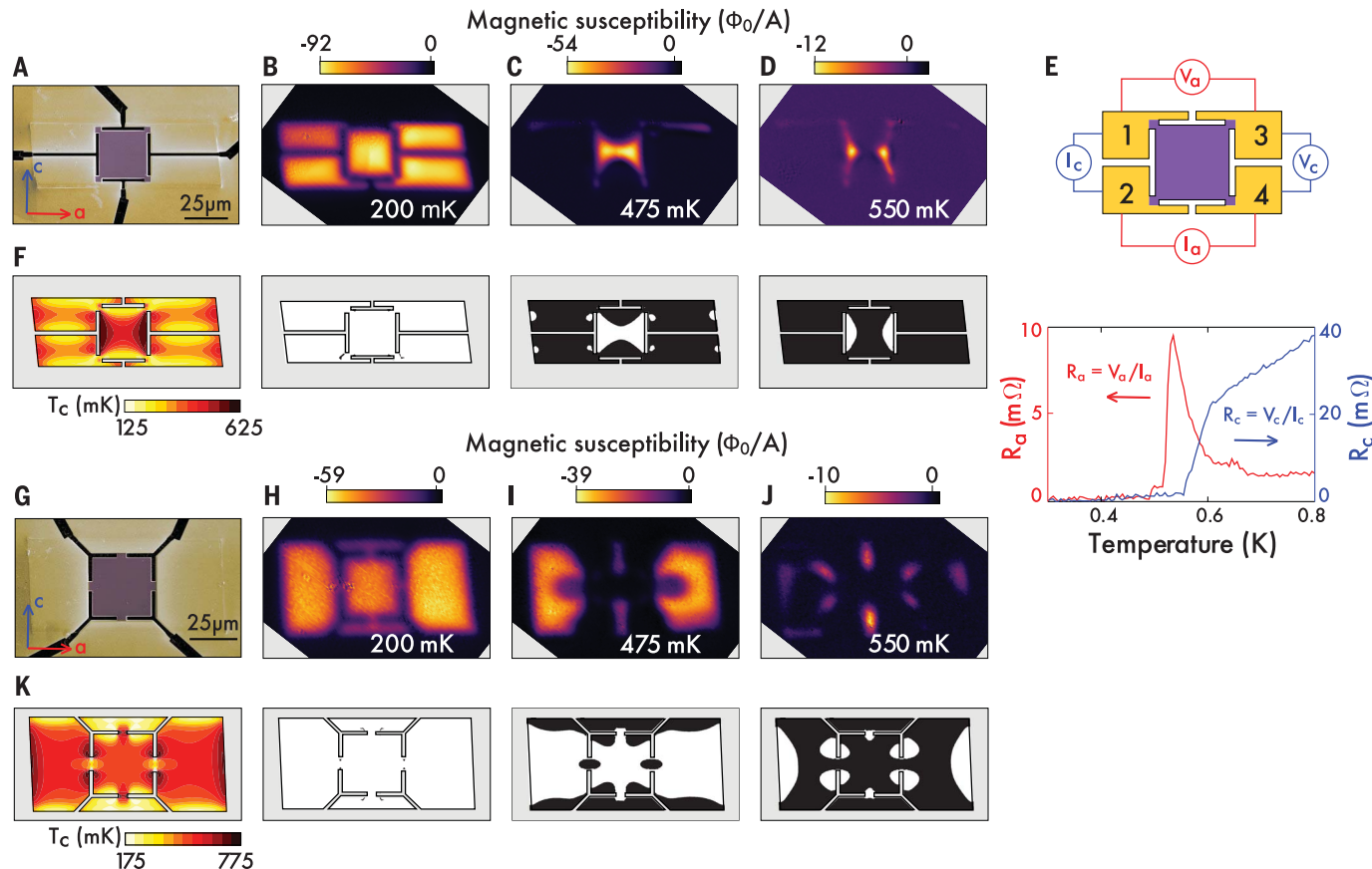


Fig. 2. Spatial control over correlations. (A) Scanning electron microscopy (SEM) image of device 1. The lamella is FIB-cut in the (a , c) plane and contacted by evaporated Au (yellow). The center square of the device is $25\ \mu\text{m}$ by $25\ \mu\text{m}$ by $3\ \mu\text{m}$, held by contacts in the corners. (B to D) (Top) Local susceptibility images at three representative temperatures illustrate the temperature evolution of the spatially modulated superconducting state. (Bottom) Calculated superconducting patterns (10). (E) Montgomery transport measurement upon cooling of device 1. As the first superconducting regions appear on the sides along the c direction (D), the c -direction resistance $R_c = V_c/I_c$ vanishes and the a -direction

resistance $R_a = V_a/I_a$ experiences a resistance spike, caused by a sudden current redistribution. I , current; V , voltage. At lower temperatures, these regions touch (C), leading to zero resistance across all contacts. (F) T_c map for device 1 from finite element calculations (10). (G) SEM image of device 2. The fabrication of device 2 was as similar as possible to that of device 1, but with the constrictions connecting at the middle of each side of the square, not the corners [compare with (A)]. (H to K) The same as in (B) to (D) and (F), but for device 2. A completely different superconducting pattern develops, as expected from the difference in position of the contacts.

of 150 GPa, this is equivalent to a uniaxial pressure of ~ 1.5 kbar, which changes T_c by ~ 100 mK (5). Hence, both the uniaxial pressure studies and the image series presented here are consistent with $\sim 0.1\%$ strain generating ~ 100 mK variation in T_c .

To understand the patterns of superconductivity, we perform finite element method simulations of the device's strain field, which is caused by the difference in the thermal contraction between CeIrIn₅ and sapphire (10). We then compute the local transition temper-

ature, T_c , from the strain field using

$$T_c = T_{c_0} + \frac{\delta T_c}{\delta \varepsilon_a} (\varepsilon_a + \varepsilon_b) + \frac{\delta T_c}{\delta \varepsilon_c} \varepsilon_c$$

for each point on the grid, resulting in a spatial T_c map (Fig. 1C). Here, ε_i with $i = a, b, c$ are the diagonal elements of the strain tensor along the corresponding crystallographic directions. We estimate $\frac{\delta T_c}{\delta \varepsilon_a} = -57$ K and $\frac{\delta T_c}{\delta \varepsilon_c} = 66$ K from reported bulk measurements of T_c as a function of uniaxial pressure, as well as our measured elastic moduli (5, 6, 10). We

generate binary images from this map, marking superconducting and metallic regions at each temperature that can be directly compared to our susceptibility images (Fig. 1, D to F). We find detailed agreement between the spatial patterns of superconducting regions observed in the SSM images at various temperatures and the pattern predicted by the simulations, which are free of fitting parameters. This agreement indicates that our modeling captures both the physical origin of the complex superconducting patches and the essence of the T_c modulation in the sample. Note that shear strains are not relevant to determine T_c for two reasons: (i) The shear strains are an order of magnitude smaller than the uniaxial strains in the lamella, and (ii) the symmetry of the superconducting order parameter in CeIrIn₅ requires that shear strain couples to T_c at higher order than the uniaxial strains [see (10) for details]. Comparison of the data and simulations shows that including these higher-order couplings is not required to model the experimental results.

Next, we show that the induced strain field and the shape of the superconducting regions can be tailored by using FIB micromachining. To define the strain field in the devices, additional trenches were cut through the lamella down to the substrate, changing the boundary conditions for the elastic equations. In both devices shown in Fig. 2, the trenches define a square in the (a, c) plane. In device 1, the square is anchored by four constrictions, one in each corner (Fig. 2A). In device 2, the constrictions connect to the center of each side of the square (Fig. 2G). Under biaxial tension, each of the contact pads is pulled outward, subjecting the square to nonuniform strain.

Device 1 is designed to measure anisotropic resistances in the plane by passing current through any pair of neighboring contacts while measuring voltage across the remaining pair (13, 14). In this device, the simulated T_c map predicts a pattern of superconductivity first developing on the edges aligned with the c direction as the device is cooled (Fig. 2F). These regions extend toward the center upon lowering the temperature, eventually connecting in the middle of the device. Such patterns are evident in the SSM images (Fig. 2, B to D) and lead to three distinct regimes for transport through device 1: (i) the normal state in which all contacts are separated by metallic regions, (ii) a state in which only the contact pairs along the c direction are connected by superconducting regions, and (iii) a state in which all contacts are connected by a single superconducting region. As a result, when current is sourced between contacts along the c direction (1 and 2), a transition to zero voltage, signaling superconductivity at a relatively high temperature T_c^* , is

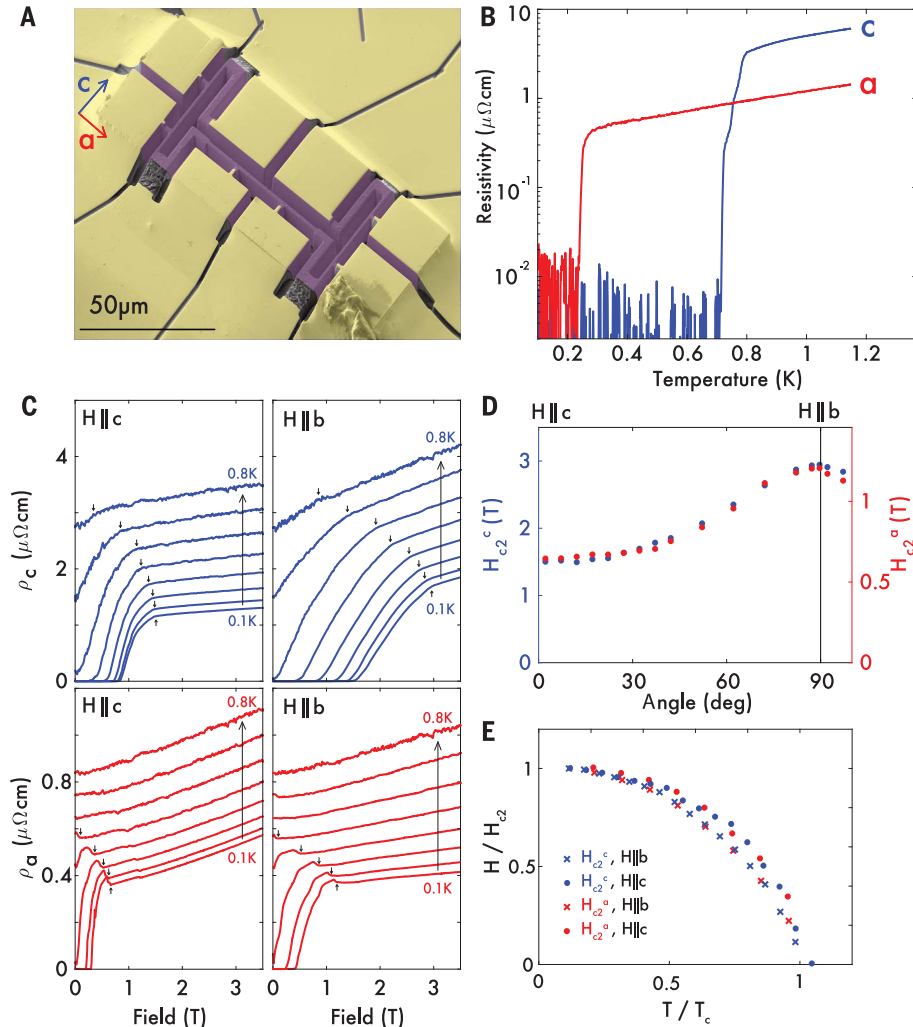


Fig. 3. Smaller structures. (A) SEM image of device 3. The device consists of long bars with dimensions $1.8 \mu\text{m}$ by $8 \mu\text{m}$ by $22 \mu\text{m}$. Two bars are oriented along the c direction and one along the a direction. (B) Resistivity as a function of temperature for device 3. Strain suppresses T_c along the bar aligned with the crystallographic a axis and enhances T_c along bars aligned with the c axis. (C) Temperature-dependent magnetoresistance along the a and c directions in CeIrIn₅ for different field orientations. All measurements were taken in a full Lorentz force configuration except ρ_c for $H\parallel c$, which is naturally longitudinal (ρ_c resistivity, H , magnetic field). (D) Angle dependence of the critical fields defined as the points where deviation from the normal magnetoresistance occurs [arrows in (C)], for both current configurations. The data collapse onto a single curve by scaling (compare the two vertical axes). (E) Temperature dependence of the critical fields for all four current and field configurations. The curves for each field configuration collapse when scaled by the respective values of $H_{c2}(0\text{ K})$ and T_c , using the experimental values for in-plane transport ($T_c \sim 0.45$ K, $H_{c2}^c\parallel b(0\text{ K}) \sim 1.2T_c$, $H_{c2}^c\parallel c(0\text{ K}) \sim 0.65T_c$) and along the c direction ($T_c^* \sim 0.8$ K, $H_{c2}^{*c}\parallel b(0\text{ K}) \sim 2.95T_c$, $H_{c2}^{*c}\parallel c(0\text{ K}) \sim 1.5T_c$).

observed (Fig. 2E, blue trace). For currents sourced between contacts along the a direction (labeled 2 and 4), we observe a sharp upturn in resistance along a , R_a , as the c -direction resistance, R_c , goes to zero (Fig. 2E). The elongated superconducting regions identified in Fig. 2D cause the current from contacts 2 to 4 to distribute evenly over the width of the device, leading to a larger current to flow at the voltage probes (labeled 1 and 3). Eventually, a second transition to a zero-resistance state occurs when all contacts are connected by a single superconducting region. The electrical response and the direct imaging of this device consistently capture the key concepts of the microscopic control over correlations: Two directed superconducting paths form in a chemically homogeneous metal, arising from the imprinted strain profile.

In contrast to those of device 1, the edges in device 2 parallel to the a axis superconduct well before the central region of the device (Fig. 2, G to K). As with device 1, we find that simulations of the strain profile in the device reproduce the structure of the superconducting transition in detail. The contrast between the two image series indicates that the structure in the images is determined by the interplay between the intrinsic strain sensitivity of the material and the strain field imposed by the FIB-defined features.

In device 2, we observe a pronounced suppression and enhancement of T_c in the a - and c -aligned constrictions, respectively. The strain in the constrictions is enhanced because the contact pads on one side and the square on the other side exert forces on the constrictions that point outward. This observation suggests a strategy to design devices that exhibit a strong modulation of T_c and to generate confined regions of suppressed superconductivity.

Smaller devices exhibit an even more pronounced dependence of the transport T_c on their geometry than larger devices. Device 3 features three series-connected straight beams with dimensions $22\ \mu\text{m}$ by $1.8\ \mu\text{m}$ by $8\ \mu\text{m}$, with two beams aligned with the c direction and one with the a direction (Fig. 3A). These fine structures cannot be resolved in detail with SSM. In transport, the transition temperature for the c -aligned beam $T_c^c \sim 700\ \text{mK}$ is higher than the bulk T_c , whereas the transition temperatures for the a -aligned beams $T_c^a \sim 200\ \text{mK}$ are considerably lower than the bulk T_c . Additional small structures show equally or even more pronounced variations of T_c (10). Therefore, a modulation of the transition temperature by more than a factor of 4 within a single crystal can be realized within our fabrication approach.

To exploit strain tuning of the superconducting order for future device-based experiments, the superconducting state must remain

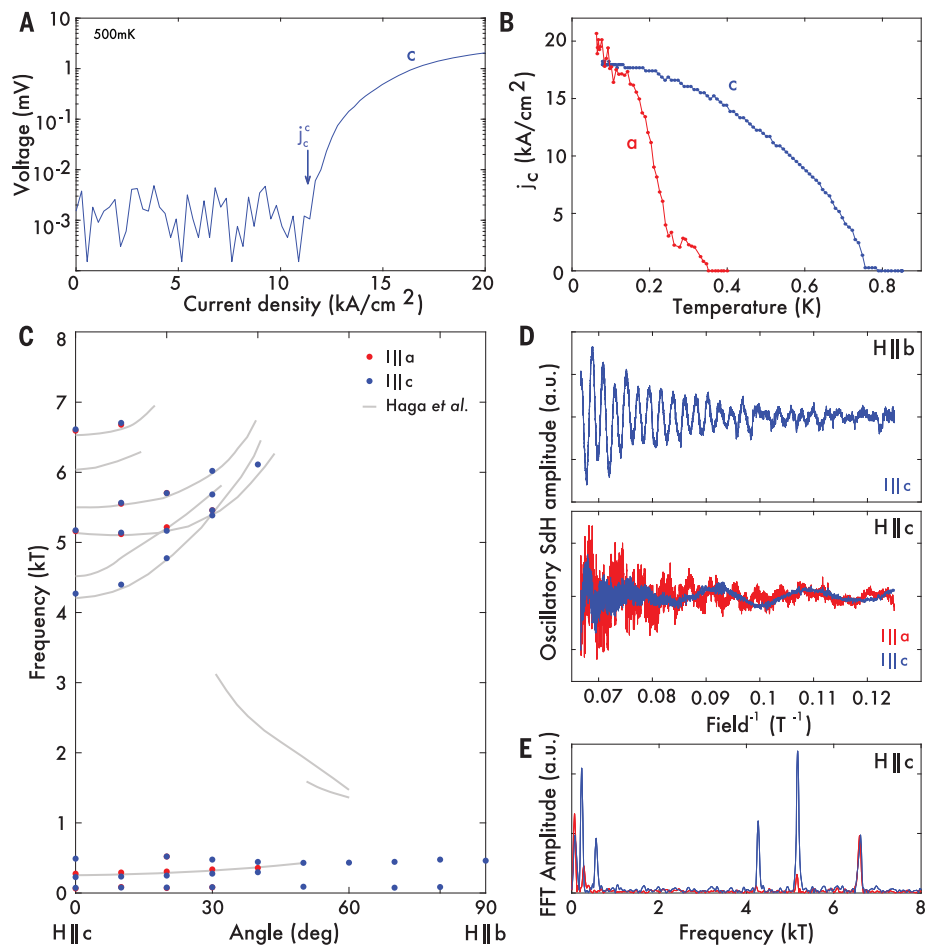


Fig. 4. Robust superconductivity coexists with quantum oscillations. (A) Current–voltage characteristic along the c direction measured on device 3 (see Fig. 3A). The onset of measurable voltage above the experimental noise level (arrow) was used to define j_c^a and j_c^c . (B) Critical current along both directions. A robust, high- j_c state is observed along the c direction, whereas the a direction is in a metallic state. (C) Angle dependence of Shubnikov–de Haas (SdH) oscillations at 80 mK measured in device 3 (points) overlaid on de Haas–van Alphen oscillations measured on bulk single crystals (gray lines) (4). (D) SdH oscillations in the microstructure for $H \parallel b$ (top) and $H \parallel c$ (bottom). a.u., arbitrary units. (E) Fast Fourier transform (FFT) spectrum for the oscillations in (D).

robust after device fabrication. To estimate the critical current of each beam, we apply high currents to device 3 (Fig. 4, A and B). The current is increased until an observable voltage signals the breakdown of the zero-resistance state. To minimize self-heating, 83- μs rectangular current pulses are applied to the sample, with a cooldown time between pulses of 100 ms. Because the critical current decreases monotonically with increasing temperature, the obtained values represent a lower bound of their magnitude in the absence of heating. Figure 4A shows a typical current–voltage characteristic of the c -aligned beam at 500 mK, well above the bulk T_c . A robust zero-resistance state is detected up to a critical current density of $\sim 12.5\ \text{kA cm}^{-2}$. Upon cooling, the critical current density increases to $j_c^c(0\ \text{K}) \sim 18\ \text{kA cm}^{-2}$ (Fig. 4B). This high critical current is typical for bulk heavy-fermion

superconductors [$\sim 3.8\ \text{kA cm}^{-2}$ for UPt_3 (15), $\sim 24\ \text{kA cm}^{-2}$ for URu_2Si_2 (15), and ~ 1 to $5\ \text{kA cm}^{-2}$ for CeCu_2Si_2 (16)], strongly supporting a scenario of robust, bulk-like superconductivity over the formation of sparse superconducting filaments under strain.

Incidentally, our observations answer an open question about the origin of the commonly observed discrepancy between thermodynamic and resistive measurements of T_c in CeIrIn_5 . Bulk crystals display a transition to a zero-resistance state well above T_c , starting as high as $T_c^* \sim 1.2\ \text{K}$ (17–19) and dependent on the details of the sample. Our results microscopically confirm proposals that strain fields around defects induce this 1 K phase (20–22). In particular, the upper critical fields H_{c2} of the strain-induced superconductivity in the microdevices can be directly scaled onto the bulk values (Fig. 3, C to E). This critical field

scaling was experimentally identified early in the study of macroscopic crystals as a hallmark signature of the 1 K phase (3). On the basis of these observations, we propose that the 1 K phase is a strain effect arising from crystal handling and wire sawing. To directly test this hypothesis, we prepared macroscopic samples by wire saw cutting. Although all samples initially had a $T_c > 1$ K, the resistive signatures of this 1 K phase are completely removed by short surface etching in HCl, after which the resistive transition coincides with thermodynamic probes at $T_c \sim 400$ mK (10). This result demonstrates the absence of defect-strained superconducting patches in single crystals of CeIrIn₅ and establishes the discrepancy between thermodynamic and resistive measurements of T_c in CeIrIn₅ as an effect of surface strain.

Here, we report a strategy to spatially modulate superconductivity within a clean electronic system that is induced by strong, nontrivial strain patterns. Spatial gradients of T_c have been generated by other methods—for example, by modulating the chemical potential across the sample by gradient doping with molecular-beam epitaxy techniques (23). In this method, variations in the local charge carrier density modify the local transition temperature. In the stoichiometric CeIrIn₅ microstructures that we studied, the charge carrier density is uniform, as evidenced by unperturbed quantum oscillations in device 3 (Fig. 4, C to E). These quantum oscillations quantitatively match the angle dependence of previously reported de Haas-van Alphen oscillations (4) measured on macroscopic crystals and indicate that the Fermi surface shape remains unchanged by the weak strain field. In particular, the large, heavy orbits and their fine structure are readily observed, which is usually very difficult in transport. This observation is incompatible with the presence of strong charge carrier density changes across the sample, which would lead to spatial variations in the Fermi surface cross sections and subsequently suppress quantum oscillations by phase smearing.

At the same time, the strain fields in device 3 are strong enough to modulate T_c by almost a factor of 4, from 200 to 780 mK. This finding suggests that the strain field spatially modulates the degree of 4f hybridization across the device and thereby also affects T_c . This mechanism, which is initially surprising, is compatible with experimental observations in the related compound CeRhIn₅ in which hydrostatic pressure suppresses antiferromagnetism and eventually induces superconductivity.

Despite the clear changes in the 4f magnetism and the spin fluctuation spectrum, the quantum oscillation frequencies remain unchanged in the entire pressure range up to the quantum critical point (24). However, the 4f hybridization increases, as evidenced by a quasiparticle effective mass that grows in response to applied pressure. This result strongly suggests that the hybridization with the 4f electrons varies without changes in the overall volume of the Fermi surface. Here we propose that the same microscopic physics underlies the spatial modulation of T_c in CeIrIn₅ microstructures.

In general, strongly correlated materials exhibit a pronounced sensitivity to perturbations, owing to the small energy scales defining their physics. The strain accessible by our fabrication approach is sufficient to substantially alter the electronic properties of these materials without introducing chemical disorder. Unlike chemical approaches to tune correlations, the FIB provides micrometer-scale control over both the direction and magnitude of the induced strain field. We expect that the approach demonstrated here will enable spatial control of a wide range of broken symmetry states in strongly correlated systems. We envision clean interfaces between regions with different electronic order within a sample generated by a spatially modulated strain field—e.g., by generating superconducting regions in structures made from antiferromagnetic CeRhIn₅ (24). Further, this approach is immediately compatible with any material that can be patterned using a FIB. Notably, although we focus on devices aligned along specific crystal axes, devices can be oriented along any direction to generate strain patterns of any desired symmetry. Strain engineering may offer an alternative way to fabricate superconducting circuitry within a metallic layer without any physical junctions, providing a route to fabricating superconductor/normal metal/superconductor Josephson junctions within a single crystal.

REFERENCES AND NOTES

1. C. W. Hicks *et al.*, *Science* **344**, 283–285 (2014).
2. A. E. Böhrer *et al.*, *Phys. Rev. Lett.* **118**, 107002 (2017).
3. C. Petrovic *et al.*, *Europhys. Lett.* **53**, 354–359 (2001).
4. Y. Haga *et al.*, *Phys. Rev. B* **63**, 060503(R) (2001).
5. O. M. Dix *et al.*, *Phys. Rev. Lett.* **102**, 197001 (2009).
6. N. Oeschler *et al.*, *Phys. Rev. Lett.* **91**, 076402 (2003).
7. R. Borth *et al.*, *Physica B* **312–313**, 136–137 (2002).
8. P. J. W. Moll *et al.*, *Nat. Commun.* **6**, 6663 (2015).
9. F. Ronning *et al.*, *Nature* **548**, 313–317 (2017).
10. See supplementary materials.
11. R. S. Kumar *et al.*, *Phys. Rev. B* **69**, 014515 (2004).
12. M. Tinkham, *Introduction to Superconductivity* (Dover, 2004).
13. H. C. Montgomery, *J. Appl. Phys.* **42**, 2971–2975 (1971).
14. L. J. van der Pauw, *Philips Tech. Rev.* **20**, 220–224 (1958).

15. S. Wüchner, N. Keller, J. L. Tholence, J. Flouquet, *Solid State Commun.* **85**, 355–360 (1993).
16. A. Pollini *et al.*, *J. Low Temp. Phys.* **90**, 15–53 (1993).
17. H. Shishido *et al.*, *J. Phys. Soc. Jpn.* **71**, 162–173 (2002).
18. T. Shang *et al.*, *Phys. Rev. B* **89**, 041101(R) (2014).
19. S. Nair *et al.*, *J. Supercond. Nov. Magn.* **22**, 195–199 (2009).
20. S. Wirth *et al.*, *J. Phys. Soc. Jpn.* **83**, 061009 (2014).
21. S. Nair *et al.*, *Phys. Rev. B* **79**, 094501 (2009).
22. A. Bianchi *et al.*, *Phys. Rev. B* **64**, 220504(R) (2001).
23. J. Wu, I. Božović, *APL Mater.* **3**, 062401 (2015).
24. H. Shishido, R. Settai, H. Harima, Y. Onuki, *J. Phys. Soc. Jpn.* **74**, 1103–1106 (2005).
25. M. D. Bachmann *et al.*, Data for “Spatial control of heavy-fermion superconductivity in CeIrIn₅,” Zenodo (2019); doi: 10.5281/zenodo.3462534

ACKNOWLEDGMENTS

We thank S. Kivelson, J. Zaanen, J. Tranquada, M. Vojta, P. Fulde, J. Thomson, S. Wirth, M. Sigrist, C. Geibel, and H. von Löhneysen for discussions and N. Nandi for low-temperature measurements.

Funding: Work at the Max Planck Institute of Chemical Physics of Solids was supported by the Max Planck Society and funded by the Deutsche Forschungsgemeinschaft (DFG, German Research Foundation) – MO 3077/1-1. Work at Cornell University was primarily supported by the U.S. Department of Energy, Office of Basic Energy Sciences, Division of Materials Sciences and Engineering, under award DE-SC0015947 (scanning SQUID imaging, implementation of millikelvin microscope). Support from the Cornell Center of Materials Research with funding from the NSF MRSEC program under award DMR-1719875 (SQUID and microscope design) is also acknowledged. T.M. is supported by the Deutsche Forschungsgemeinschaft through SFB 1143 and the Emmy Noether-Programme via grant ME 4844/1-1. M.D.B. acknowledges studentship funding from EPSRC under grant EP/1007002/1. P.J.W.M. was supported by the European Research Council (ERC) under the European Union’s Horizon 2020 research and innovation program (GA 715730). R.D.M. and L.E.W. acknowledge funding support from the National High Magnetic Field Laboratory, which is supported by NSF Cooperative Agreements DMR-1157490 and DMR-1644779, as well as the state of Florida and the U.S. Department of Energy. E.H. and F.A. acknowledge funding from the Max Planck Society for the research group “Physics of Unconventional Metals and Superconductors.” Work at Los Alamos National Laboratory was performed under the auspices of the U.S. Department of Energy, Office of Basic Energy Sciences, Division of Materials Sciences and Engineering.

Author contributions: M.D.B., K.A.M., M.K., C.P., and P.J.W.M. fabricated the microstructures; M.D.B., T.H., K.R.S., K.A.M., Y.-S.L., M.N., C.P., and P.J.W.M. performed the transport measurements; G.M.F. performed the scanning SQUID imaging with support from D.L. and K.C.N.; F.T. and G.M.F. performed the finite element simulations with input from K.C.N. and B.J.R.; E.D.B. and F.R. grew the crystals; T.M. contributed the theoretical treatment; F.A., E.H., and M.D.B. performed the magnetotransport measurements in the dilution refrigerator; R.D.M. and L.W. measured simultaneous transport in liquid ³He; and all authors contributed to the experiment design and manuscript writing. **Competing interests:** The authors declare no competing interests. **Data and materials availability:** All experimental data shown in the main text and supplementary materials are available at Zenodo (25). The simulations of the strain fields were performed using COMSOL Multiphysics. The COMSOL workbooks used for this work are also available at Zenodo (25).

SUPPLEMENTARY MATERIALS

science.sciencemag.org/content/366/6462/221/suppl/DC1
Materials and Methods
Supplementary Text
Figs. S1 to S13
Tables S1 and S2
References (26–37)

13 August 2017; resubmitted 20 September 2018
Accepted 12 September 2019
10.1126/science.aao6640

Spatial control of heavy-fermion superconductivity in CeIrIn₅

Maja D. Bachmann, G. M. Ferguson, Florian Theuss, Tobias Meng, Carsten Putzke, Toni Helm, K. R. Shirer, You-Sheng Li, K. A. Modic, Michael Nicklas, Markus König, D. Low, Sayak Ghosh, Andrew P. Mackenzie, Frank Arnold, Elena Hassinger, Ross D. McDonald, Laurel E. Winter, Eric D. Bauer, Filip Ronning, B. J. Ramshaw, Katja C. Nowack and Philip J. W. Moll

Science **366** (6462), 221-226.
DOI: 10.1126/science.aao6640

Modulating superconductivity

Strain can have considerable effects on the electronic properties of materials. For instance, the temperature at which a material becomes superconducting—the critical temperature—can be tuned by varying strain. Bachmann *et al.* used focused ion beam milling to fabricate microstructures of the superconductor CeIrIn₅ on sapphire substrate. A difference in the thermal contraction coefficients of the two layers induced nonuniform strain upon cooling of the sample, leading to large gradients of the critical temperature. This approach can be used in other materials and may enable fabrication of superconducting circuitry without physical junctions.

Science, this issue p. 221

ARTICLE TOOLS

<http://science.sciencemag.org/content/366/6462/221>

SUPPLEMENTARY MATERIALS

<http://science.sciencemag.org/content/suppl/2019/10/09/366.6462.221.DC1>

REFERENCES

This article cites 35 articles, 2 of which you can access for free
<http://science.sciencemag.org/content/366/6462/221#BIBL>

PERMISSIONS

<http://www.sciencemag.org/help/reprints-and-permissions>

Use of this article is subject to the [Terms of Service](#)

Science (print ISSN 0036-8075; online ISSN 1095-9203) is published by the American Association for the Advancement of Science, 1200 New York Avenue NW, Washington, DC 20005. The title *Science* is a registered trademark of AAAS.

Copyright © 2019 The Authors, some rights reserved; exclusive licensee American Association for the Advancement of Science. No claim to original U.S. Government Works